Impacts of T-type Intersections on the Connectivity and Flow in Complex Fracture Networks

Weiwei Zhu[1], Zhiqiang Chen[1], Yafan Yang[2], Wenbo Gong[3], and Moran Wang[1]

[1]Tsinghua University
[2]China University Of Mining And Technology, Xuzhou
[3]China University of Mining & Technology

November 23, 2022

Abstract

T-type intersections are commonly observed in natural fracture networks. Their impacts on the connectivity and flow results in complex fracture networks are rarely investigated. In this work, we implement the discrete fracture network method to construct complex fracture networks, denoted as original fracture networks. By implementing the rule-based fracture growth algorithm, we generate the corresponding kinematic fracture networks with a substantial proportion of T-type intersections. The connectivity and flow results of both the single-phase and two-phase flow simulations in these two types of fracture networks are systematically investigated. The results show that kinematic fracture networks tend to connect more fractures with fewer intersections and yield better connectivity than the original ones. Most kinematic fracture networks have larger permeability in the single-phase flow simulation and higher cumulative gas production in the two-phase flow simulation than original fracture networks under the same boundary conditions. The proportions of permeability and production enhancement are 68\% and 77\%, respectively. Flow results, like the permeability and production, have strong positive correlations with the connectivity of the fracture networks, but they are nonequivalent and strongly impacted by the number of inlets and outlets.

Impacts of T-type Intersections on the Connectivity and Flow in Complex Fracture Networks

Weiwei Zhu[1], Zhiqiang Chen[2], Yafan Yang[3], Wenbo Gong[1], Moran Wang[1]

[1]Department of Engineering Mechanics, Tsinghua University, Beijing, China
[2]Petroleum Exploration and Production Research Institute, SINOPEC, Beijing, China
[3]State Key Laboratory for Geomechanics and Deep Underground Engineering, China University of Mining and Technology, Xuzhou, China

Key Points:

- The rule-based fracture growth algorithm is implemented to construct kinematic fracture networks with substantial T-type intersections.
- Impacts of T-type intersections on the connectivity of complex fracture networks are systematically investigated.
- Impacts of T-type intersections on the single/two-phase flow in complex fracture networks are systematically investigated.

Corresponding author: Moran Wang, mrwang@tsinghua.edu.cn

Abstract

T-type intersections are commonly observed in natural fracture networks. Their impacts on the connectivity and flow results in complex fracture networks are rarely investigated. In this work, we implement the discrete fracture network method to construct complex fracture networks, denoted as original fracture networks. By implementing the rule-based fracture growth algorithm, we generate the corresponding kinematic fracture networks with a substantial proportion of T-type intersections. The connectivity and flow results of both the single-phase and two-phase flow simulations in these two types of fracture networks are systematically investigated. The results show that kinematic fracture networks tend to connect more fractures with fewer intersections and yield better connectivity than the original ones. Most kinematic fracture networks have larger permeability in the single-phase flow simulation and higher cumulative gas production in the two-phase flow simulation than original fracture networks under the same boundary conditions. The proportions of permeability and production enhancement are 68% and 77%, respectively. Flow results, like the permeability and production, have strong positive correlations with the connectivity of the fracture networks, but they are nonequivalent and strongly impacted by the number of inlets and outlets.

1 Introduction

Fractures provide essential pathways to subsurface flow in formations with low permeability [*Berkowitz*, 2002; *Hardebol et al.*, 2015; *Gierzynski and Pollyea*, 2017]. However, current technologies, such as outcrop observations, wellbore imaging, seismic mapping, and crosswell seismic techniques [*Rijks and Jauffred*, 1991; *Wilt et al.*, 1995; *Ellefsen et al.*, 2002; *Prioul and Jocker*, 2009; *Ukar et al.*, 2019], are insufficient to have detailed characterizations of subsurface fracture networks. Discrete fracture networks (DFNs) are a practical alternative to describe subsurface fractures by preserving main geometrical properties, such as fracture lengths, center positions, orientations, and topological structures, but neglecting intricate details, like fracture roughness and curved shapes. DFNs are widely used to investigate the natural fracture networks and their impact on the subsurface flow [*Robinson*, 1983; *Bour and Davy*, 1997a, 1998; *Darcel et al.*, 2003; *Wang et al.*, 2007; *Lei et al.*, 2017; *Zhu et al.*, 2018; *Wang et al.*, 2021].

The ordinary procedure to generate DFNs includes: i, choosing proper stochastic distributions to describe fracture geometries; ii, generating discrete fractures according to the chosen distribution in succession; iii, stopping generating fractures when the termination criterion is reached, such as a prescribed fracture intensity. Through implementing the procedure, it is almost impossible to generate fractures abutting the other fractures (T-type intersections, Fig. 1a), and only cross fractures (X-type intersections, Fig. 1b) are available. However, T-type intersections are commonly observed in real outcrop maps and take a significant proportion of the total intersections [*Dershowitz and Einstein*, 1988; *Watkins et al.*, 2015; *Zhu et al.*, 2021a]. Fig. 2 shows two fracture outcrop maps at the Achnashellach Culmination field area in North-West Scotland (Fig. 7B and 7D in *Watkins et al.* [2015]), and different types of nodes are marked in different colors. The proportions of T-type intersections are 74% and 76%, respectively. V-type intersections (Fig. 1c) have coincident tips and are unlike to form in reality [*Sanderson and Nixon*, 2015]. Therefore, they are not distinguished from T-type intersections in Fig. 2.

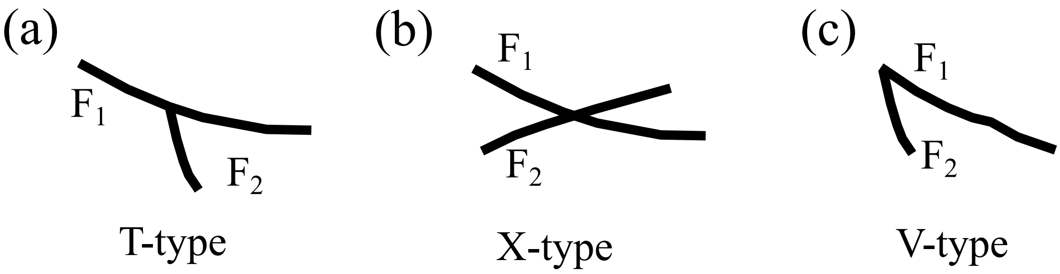

Figure 1. Demonstration of different types of intersections between fractures. F_1 and F_2 refer to the first and second fracture.

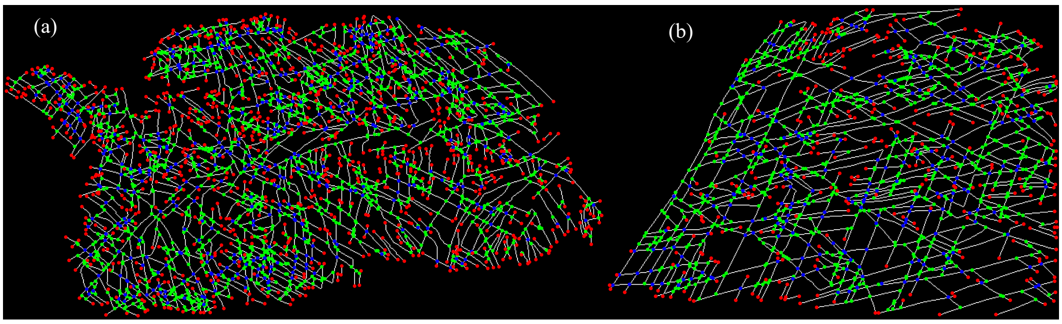

Figure 2. Fracture outcrop map at Achnashellach Culmination field area in North-West Scotland (Fig. 7B and 7D in *Watkins et al.* [2015]) with different types of intersection nodes marked in different colors. Red nodes are isolated nodes; Green nodes refer to T-type intersection nodes; Blue nodes represent X-type intersection nodes.

T-type intersections are naturally formed during the fracture growth process, and they are important to enhance the connectivity of fracture networks because of the reduction of dead-ends [*Barton and Hsieh*, 1989; *Odling*, 1997]. Complex Numerical schemes are necessary to obtain the accurate stress/strain field considering different rock types, strengths, and stress states [*Olson et al.*, 2009; *Chen and Wang*, 2017]. However, in complex fracture networks, such numerical simulation is computationally unacceptable. Therefore, detailed investigations on the impact of T-type intersections on the connectivity and subsurface flow in complex fracture networks are rarely conducted.

Davy et al. [2010, 2013] considered the fracture growth process by simplifying the complex mechanical calculation with three steps: nucleation, growth, and arrest. The method provides different constraining rules according to field and experiment observations and mechanical principles to describe the nucleation, growth, and arrest process. The rule-based method renders main mechanical interactions and forms many T-type intersections. *Maillot et al.* [2016] implemented the nucleation-growth-arrest method and investigated the impact of T-type intersections on fracture connectivity and flow, where meaningful findings and conclusions were summarized. However, their cases are limited to comparisons between the kinematic and Poisson models, where fracture centers and fracture orientations are uniformly distributed. Percolation analysis was involved, and the conventional percolation threshold derived from excluded volume method is only applicable for the Poisson model dominated by small fractures [*Bour and Davy*, 1997a; *Zhu et al.*, 2018]. However, natural fractures are usually spatially clustered instead of uniform [*Akara et al.*, 2021; *Zhu et al.*, 2018] and preferential orientations depending on stress history are commonly observed [*Laubach*, 1988; *Kemeny and Post*, 2003; *Watkins et al.*, 2015]. Therefore, a more systematic analysis is necessary to investigate the impact of T-type intersections on the connectivity and subsurface flow in complex fracture networks.

In this work, we followed the rule-based nucleation-growth-arrest method to generate T-type intersections in complex fracture networks, considering a wide range of geometrical variations on fractures. In specific, different levels of fracture lengths, orientations, and clustering degrees are included to describe complex fracture networks. Two types of fracture networks are constructed for comparison: original fracture networks (no fracture growth algorithm implemented) and kinematic fracture networks (with fracture growth algorithm implemented). Impacts of T-type intersections on the connectivity and subsurface flow are then systematically investigated in complex fracture networks.

The organization of this paper is as follows: In Section 2, techniques to construct complex fracture networks and generate T-type intersections are introduced. Topology analysis and flow simulation details are also included in Section 2. In Section 3, results of the systematic analysis of two types of fracture networks are presented. The impact of T-type intersections on the connectivity and subsurface flow is analyzed in detail. Section 4 summarizes important findings and conclusions.

2 Materials and Methods

In this section, we introduce techniques to construct complex fracture networks and their corresponding kinematic fracture networks considering the fracture growth process. The detailed information for the single and two-phase flow simulation is also presented.

2.1 Fracture network construction and topology analysis

The process to construct discrete fracture networks are intensively discussed, and details are available in our recent preprint on the in-house DFN modeling software, HatchFrac [*Zhu et al.*, 2021b]. Three main geometrical properties of fractures are emphasized in this work and described with different stochastic distributions. A power-law distribution is adopted to describe fracture length [*Bour and Davy*, 1997b]. The fracture orientations are characterized by the von Mises–Fisher distribution [*Whitaker and Engelder*, 2005]. The fractal spatial density distribution is implemented to generate clustered fracture centers, which is closer to the reality [*Akara et al.*, 2021; *Zhu et al.*, 2021a]. A fractal dimension characterizes the fractal spatial density distribution and varies between 1.0 and 2.0 for fracture networks in 2D. The system size is 100 arbitrary units, and the minimum length of fractures is 10 units. From outcrop observations, the exponent of the power-law usually varies in the range of [2.0, 3.0] [*Bonnet et al.*, 2001; *Zhu et al.*, 2018] and the concentration parameter κ is usually smaller than 3.0 [*Zhu et al.*, 2021a]. In this work, three levels of each parameter are chosen to represent different scenarios of complex fracture networks. A Taguchi method [*Karna et al.*, 2012] is adopted to generate nine orthogonal cases with three levels for three parameters. Each case is stabilized with 10 realizations to avoid random effects from statistic distributions. Although this work focuses on the analysis of the 2D fracture network, the extension to 3D fracture networks can be convenient following similar procedures in 2D cases. Table 1 summarizes the parameters for each case.

Table 1. Parameters for complex fracture networks

Parameter	Low	Intermediate	High	Definition
Fracture length, a	2.0	2.5	3.0	The exponent of a power-law distribution
Position of the fracture center, F_D	1.5	1.7	2.0	The fractal dimension of a fractal spatial density distribution
Fracture orientation, κ	0	5	10	The concentration parameter in a von Mises–Fisher distribution

After choosing the parameters for different statistic distributions, the discrete fracture network can be constructed by adding fractures in succession. The termination criterion is when the fracture network is over-percolative, and the fracture intensity is twice as large as the intensity at the percolation state. The percolation state is where a spanning cluster connecting four sides of the domain is formed. The over-percolative states are widely observed from natural outcrops [*Watkins et al.*, 2015; *Zhu et al.*, 2021a]. 90 discrete fracture networks are generated and denoted as original fracture networks since no fracture growth is considered. Fracture networks considering fracture growth are denoted as kinematic fracture networks.

Connectivity determines the hydraulic diffusivity of a fracture network and significantly impacts the flow behavior. Several methods are available to measure connectivity of the fracture system, such as the connectivity index/field method [*Xu et al.*, 2006; *Fadakar-A et al.*, 2013], global efficiency method [*Zhu et al.*, 2021c], ternary diagram method [*Barton and Hsieh*, 1989]. Aperture variations of fractures are not included in this work. Therefore, it is sufficient and convenient to follow *Sanderson and Nixon* [2015] and adopt C_B, the mean number of linkages of each branch, as the measure of connectivity.

$$C_B = \frac{3 \times N_T + 4 \times N_X}{N_B}, \tag{1}$$

where $\mathrm{N_T}$, $\mathrm{N_X}$, and $\mathrm{N_B}$ refer to the numbers of T-type nodes, X-type nodes and branches. $\mathrm{N_B}$ is calculated by:

$$N_B = \frac{1}{2}(N_I + 3N_T + 4N_X), \tag{2}$$

where N_I is the number of I-type nodes.

C_B is a dimensionless number varying between 0 and 2.0, and a larger value indicates better connectivity. The topology analysis and connectivity index calculation are conducted for the largest cluster of the fracture network (red fractures in Fig. 3) instead of all fractures because the subsurface fluid flows through well-connected fracture networks instead of isolated fractures in formations with low permeability.

Figs. 3(a) and (b) show two examples of original fracture networks with different combinations of geometrical parameters. The fracture network in Fig. 3(a) has $a = 3, F_D = 2$, and $\kappa = 5$. The total amount of intersections in the largest fracture cluster is 1210. The connectivity index is 1.724. The fracture network in Fig. 3(b) has $a = 2, F_D = 1.5$, and $\kappa = 0$. The total number of intersection and the connectivity index of the largest cluster are 522 and 1.80 respectively.

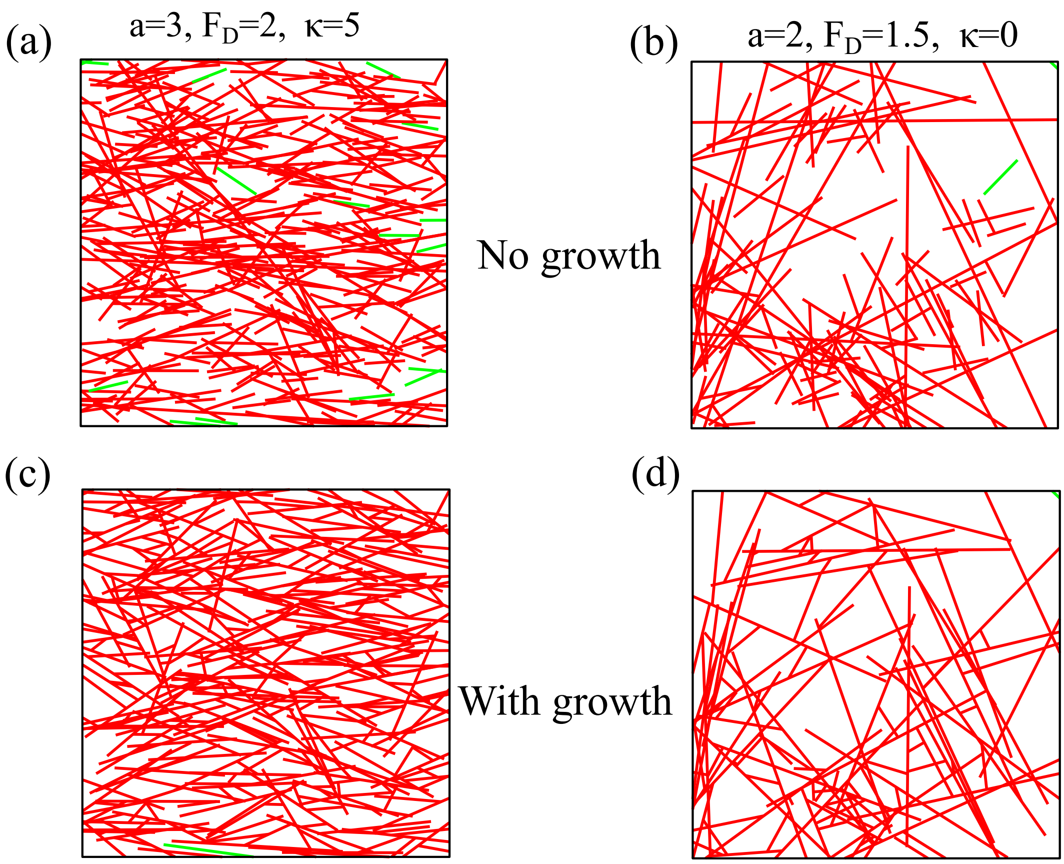

Figure 3. Examples of the original fracture networks (a, b) and the corresponding kinematic fracture networks (c,d). Red line segments refer to the largest fracture cluster and green line segments are local clusters.

2.2 Fracture growth and T-type intersections

The rule-based fracture growth algorithm constrains the growth process with specific nucleation, growth, and arrest rules. Making original and kinematic fracture networks similar is essential to compare their impacts on connectivity and flow results. Therefore, we construct a corresponding kinematic counterpart for each original fracture network. The number of nuclei equals the number of fractures in the original fracture network. Each nucleus grows in the same direction as the original fracture. The fracture intensity, P_{21} (the length of fracture traces per unit area), is kept the same for the original and kinematic fracture networks. Therefore, the kinematic fracture network requires one degree of freedom to match the prescribed intensity. Fracture lengths in kinematic fracture networks vary to match the intensity and depend on the velocity model and arrest criterion. The arrest criterion is that each fracture tip stops growing when it encounters a large fracture [*Segall and Pollard*, 1983; *Nur*, 1982]. The growth velocity at fracture tips follows a power-law distribution if assuming fracture propagation happens in a stable and quantifiable sub-critical regime [*Olson*, 2004; *Engelder*, 2004].

$$v = dl/dt = \mathrm{A}(\frac{\mathrm{K_I}}{\mathrm{K_{IC}}})^n \tag{3}$$

where $\mathrm{K_I}$ is a stress intensity factor of the opening mode at the fracture tip; $\mathrm{K_{IC}}$ is the fracture toughness at opening mode; A is a proportionality coefficient. n is a sub-critical growth index of the fracture, depending on environmental conditions and rock types. For simplicity, we set $n = 0$ and assume the growth velocity of the i^{th} fracture is a combination of a constant part and a length-related random part.

$$v_i = l_c + \mathrm{rand}(0, 2.0 \times \frac{\mathrm{l_i}}{\mathrm{l_{max}}}) \tag{4}$$

where l_c is the constant velocity for all fractures and set as 5 units/step; $\mathrm{rand(a, b)}$ is a function to generate random varaibles distributed in the interval $[a, b]$; l_i is the length of original fracture; l_{max} is the largest fracture length in the original fracture network. The advantage of Eq. 4 is to provide a degree of freedom with the random function to match the prescribed fracture intensity. Furthermore, larger fractures in the original fracture network tend to have a higher growth velocity and remain a similar shape in the kinematic fracture network. Choices of l_c and the coefficient of 2.0 before $\frac{l_i}{l_{max}}$ are decided with trial and error and the chosen combination can reach the convergence efficiently.

Figs. 3(c) and (d) show the corresponding kinematic fracture networks of Figs. 3(a) and (b). The total number of intersections in the largest fracture cluster of the fracture network in Fig. 3(c) is 1150, and the connectivity index is 1.827. For the fracture network in Fig. 3(d), the total number of intersections and the connectivity index of the largest cluster are 450 and 1.877, respectively.

2.3 Single/two-phase flow simulation

We consider the impact of T-type intersections in the single-phase and two-phase flow, which are essential for real engineering applications. The enhanced geothermal extraction process is a typical simplified single-phase flow example, where cold water is injected into the subsurface formation and transported to the production well through the fracture network. A two-phase flow simulation can mimic the simplified process of shale gas production, where natural gas stored in the matrix firstly flows to the fracture network and then to the production well. UNCONG[*Li et al.*, 2015] is adopted to simulate the single/two-phase flow with embedded discrete fracture network techniques. In the flow simulation, the unit of the system size is a meter for convenient calculations.

For the single-phase flow simulation, the matrix is assumed to be impermeable and constant pressure boundary conditions are implemented for all fracture networks. The inlet boundary (left side) has a constant pressure of 2.0 bar, and the outlet boundary (right side) has a constant pressure of 0 bar. The chosen pressure values constrict the Reynolds number to a feasible range, $\mathcal{O}(10^{-3})$ and yield a macroscopic pressure gradient of 2.0 kPa/m [*Zhu et al.*, 2021c]. The top and bottom boundaries are set impermeable. A sketch map of the boundary condition for the single-phase flow is demonstrated in Fig. 4(a). Fig. 5(a) shows the pressure distribution of the single-phase flow in the fracture network (Fig. 3(a)).

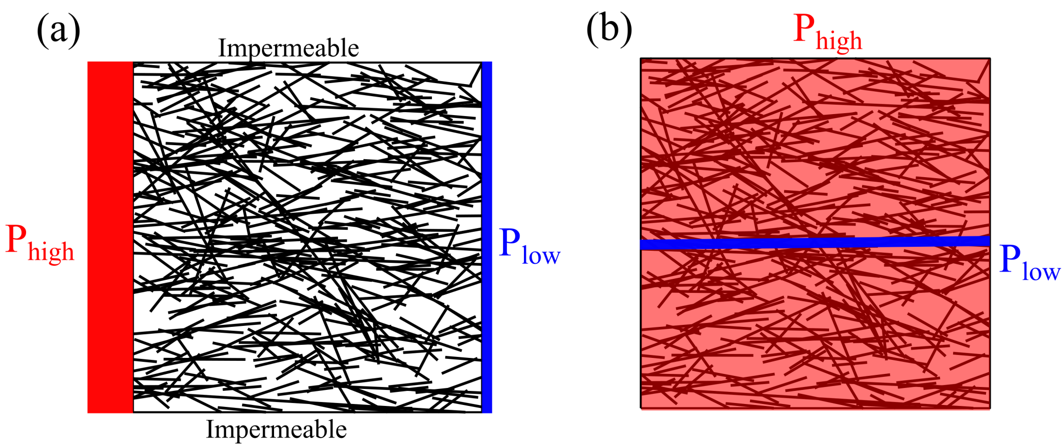

Figure 4. Boundary conditions for the single-phase (a) and two-phase (b) flow

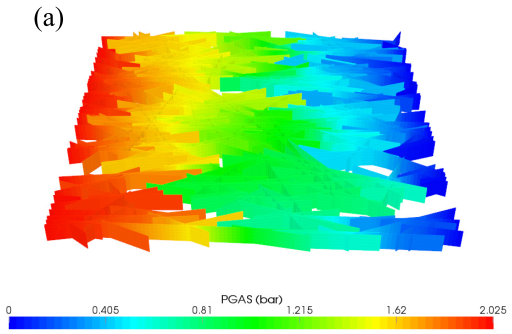

Figure 5. Pressure distribution in the single-phase flow simulation (a) and two-phase flow simulation (b)

For the two-phase flow, we consider the gas-water flow in formations with ultra-low permeability. The matrix has a low permeability of 1.0 micro-darcy. Fractures have a high permeability of 10 darcies, seven orders of magnitude higher than the matrix permeability. The initial reservoir pressure is set as 300 bar. A horizontal well is drilled at the middle of the formation, and the bottom-hole pressure is set as 100 bar and kept constant. Fig. 4(b) presents a sketch map of the boundary condition for the two-phase flow. Detailed input parameters are listed in Table 2. Fig. 6(a) shows the compressibility and viscosity changes of gas with pressure. Figs. 6 (b) and (c) show the relative permeability curves in the matrix and fractures, respectively. The production is simulated for ten days, and Fig. 5(b) shows the pressure distribution in the formation after the production.

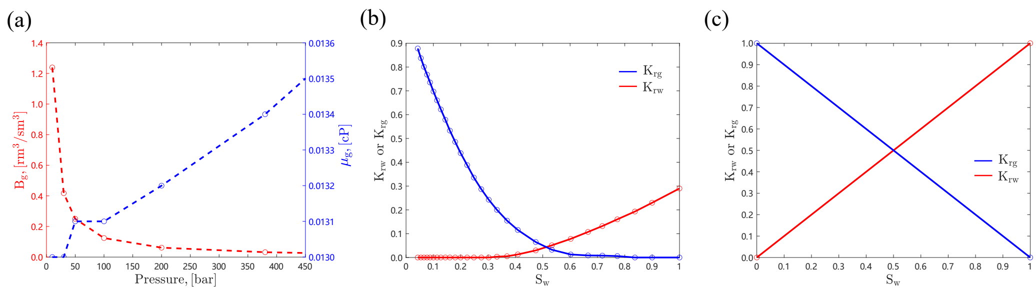

Figure 6. (a) the compressibility (B_g) and viscosity (μ_g) changes of gas with pressure; (b) the relative permeability curve in the matrix; (c) the relative permeability curve in fractures; After *Zhu et al.* [2022].

Table 2. Input parameters for the two-phase simulation

Property	Value
Matrix permeability, k_m [μd]	1.0
Matrix porosity, ϕ_m [-]	0.05
Fracture permeability, k_f [d]	10
Fracture porosity,ϕ_f [-]	1.0
The coefficient of water compressibility,B_w [bar^{-1}]	3.15e-6
The coefficient of water viscosity compressibility, $B\mu_w$ [cP $\cdot$ bar^{-1}]	2.10e-6
Initial water saturation, S_{wi} [-]	0.5
Initial reservoir pressure, P_i [bar]	300
Constant bottomhole pressure, P_b [bar]	100

3 Results and discussion

The corresponding kinematic fracture networks share the same orientations and fracture intensities, both P_{20} and P_{21}, as the original fracture networks. However, 87 out of 90 kinematic fracture networks show different length distributions from the original ones based on a Two-sample Kolmogorov-Smirnov test, which is necessary to match the prescribed fracture intensity.

Fig. 7 shows the proportion of T-type intersections out of total intersections. Almost no T-type intersections exist in the original fracture networks, and the corresponding proportion is close to zero for all scenarios (blue circles). After implementing the fracture growth algorithm, the proportion of T-type intersections is significantly increased (red circles), and the mean proportion of the 90 scenarios is 0.32.

Fig. 8 shows the ratio of the total number/ length of fractures in the largest cluster and the whole domain in both kinematic and original fracture networks. Green line segments linking two fracture networks represent an increase from the original case to the corresponding kinematic case, and black line segments denote a decrease. All cases have more fractures belonging to the largest cluster in the kinematic fracture networks than the original ones. 4 out of 90 cases have larger fracture lengths in the original fracture networks than in the kinematic ones. Fig. 9 shows the ratios of total intersections and connectivity index between the kinematic and original fracture networks. Most cases have better connectivity in the kine-

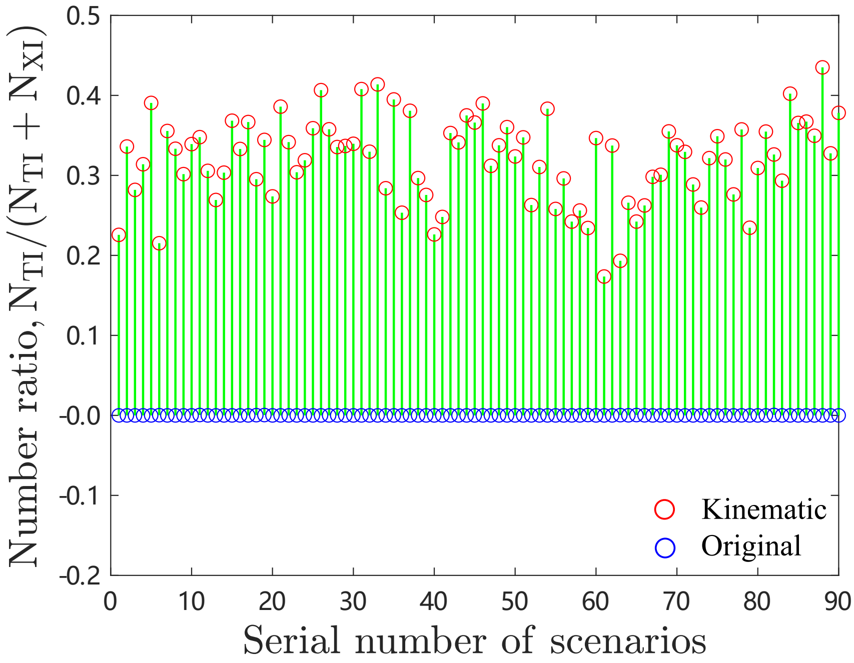

Figure 7. The ratio between the number of T-type intersections (N_{TI}) and total intersections (T-type, N_{TI} plus X-type, N_{XI})

matic than the original fracture networks. The only different case also has its connectivity index ratio close to 1.0. Most of the scenarios (77 out of 90) have fewer intersections in the kinematic than the original fracture networks. The decreasing intersections and increasing fracture numbers yield a decreasing intersections per fracture (I_{pf}) in the kinematic fracture networks. I_{pf} has been adopted as a percolation parameter and a measure of connectivity for fracture networks with constant fracture lengths and uniformly distributed fracture centers and orientations [*Robinson*, 1983]. However, the results here demonstrate that I_{pf} is an invalid parameter to characterize the connectivity of complex fracture networks as concluded in *Zhu et al.* [2018]. In a kinematic fracture network with substantial T-type intersections, the connectivity is enhanced, and more fractures are connected to form a larger cluster, but the number of intersections usually decreases.

From the single-phase flow simulation, the permeability of the fracture network is calculated. Fig. 10 shows the ratio of permeability between kinematic and origin fracture networks. Out of 90 cases, 61 cases have their permeability increased in the kinematic fracture networks compared with the original ones. The maximum increase of permeability can be 3.5 times. Different fracture geometries (fracture length, positions, and orientations)

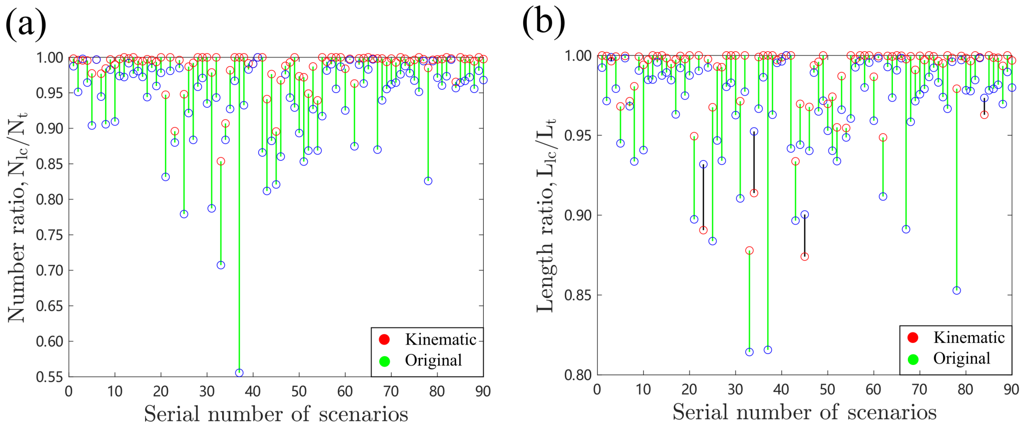

Figure 8. Ratios between the number (a) and length (b) of fractures in the largest cluster(N_{lc}, L_{lc}) and the number and length of total fractures(N_t, L_t)

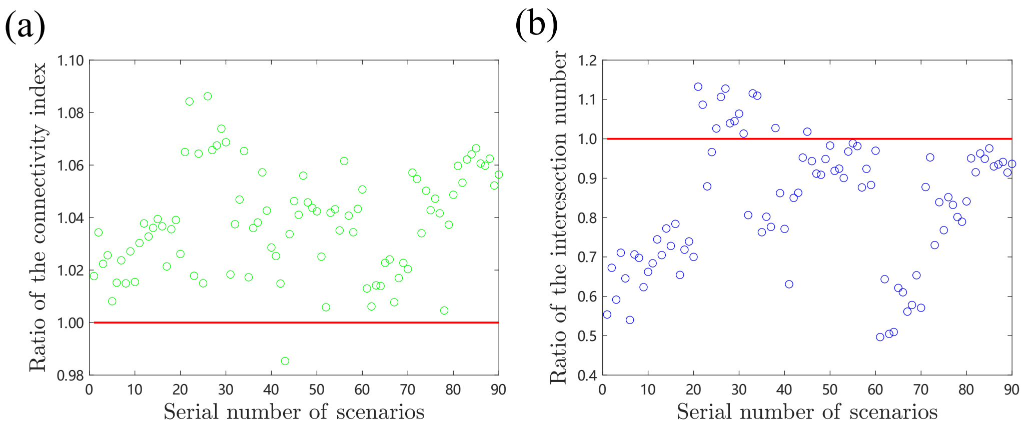

Figure 9. Ratios of the connectivity index (a) and total number of intersections (b) between the kinematic and original fracture networks

have a different impact on the permeability ratio. Therefore, results are plotted separately in different colors and sub-figures regarding fracture length (a), positions of fracture centers (F_D), and concentrated fracture orientations (κ). The number of cases with a permeability ratio larger than 1.0 is denoted in the figure. From Fig. 10 (a), more cases have a higher permeability in the kinematic fracture networks with an increase of a, indicating that kinematic fracture networks composed of small fractures tend to have better permeability. The clustering effects have a negative contribution to the permeability enhancement in the kinematic fracture networks, as shown in Fig. 10 (b). Fig. 10 (c) shows non-monotonic variations of concentrate fracture orientations on the permeability ratio, indicating an insignificant impact from the orientation concentration on the permeability enhancement.

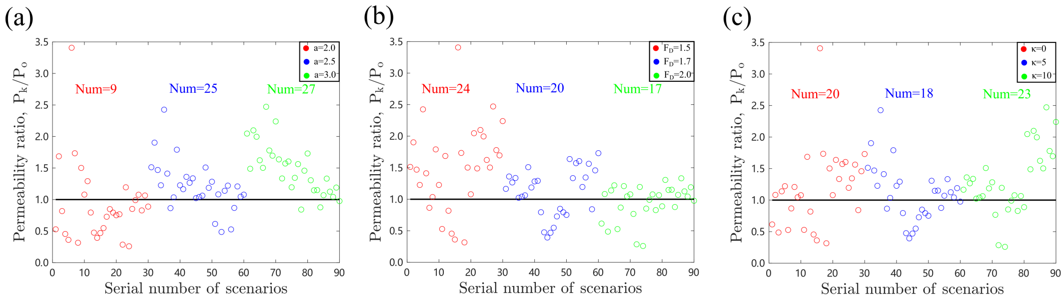

Figure 10. Permeability ratio between the kinematic fracture networks and the original ones. Different sub-figures classify the permeability ratio based on the geometrical parameters: (a) the power-law exponent a; (b) the fractal dimension F_D; (c) the concentration parameter κ. The number of cases with the ratio larger than 1.0 is denoted.

An input/output correlation method is implemented to evaluate the impact of each independent geometrical parameter on the permeability of kinematic and original fracture networks. The sensitivity of each parameter is measured according to the correlation coefficient, ρ, between the parameter and the response. Fig. 11 shows the sensitivity analysis of fracture geometries with different responses, including the permeability of original fracture networks (Fig. 11a), the permeability of kinematic fracture networks (Fig. 11b), and the permeability ratio between these two types of fracture networks (Fig. 11c). For the original and kinematic fracture networks, both a and κ have positive correlations with the permeability, indicating that fracture networks composed of small fractures with concentrated orientations tend to have higher permeability. The orientation concentration has a more critical impact on the permeability enhancement. F_D has slightly negative correlations, indicating that clustering effects can enhance permeability and this effect is more significant in kinematics fracture networks. a and F_D have positive and negative correlations with the permeability ratio. κ has an insignificant impact on the permeability ratio. The correlation results in Fig. 11(c) are consistent with behaviors shown in Fig. 10.

Fig. 12 shows ratios of cumulative gas production after ten days between kinematic and original fracture networks. In all 90 cases, 69 cases have their cumulative production larger in the kinematic fracture networks than in the original ones. The maximum increase can be 1.4 times. Different sub-figures and colors are presented for different geometrical parameters (a, F_D, and κ). a and F_D have positive and negative impacts on the production ratio, similar to the results in the permeability ratio in Figs. 10(a, b). Therefore, kinematic fracture

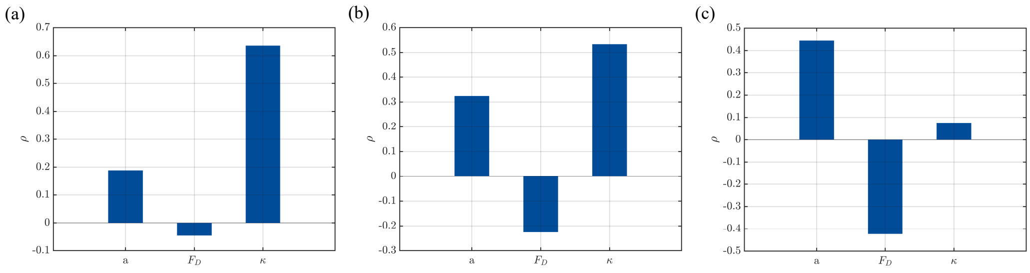

Figure 11. Sensitivity analysis of fracture geometries with (a): permeability in origin fracture networks; (b): permeability in kinematic fracture networks; (c): permeability ratio between kinematic and original fracture networks as responses. ρ is the correlation coefficient between the parameter and the response.

networks that are composed of small fractures (a larger exponent, a) with weak clustering effects (a larger fractal dimension, F_D) tend to produce more than the original ones. The concentration parameter κ has a negative impact on the production ratio instead of non-monotonic variations shown in Fig. 10(c), indicating that concentrated fracture orientations may not help to enhance production in kinematic fracture networks.

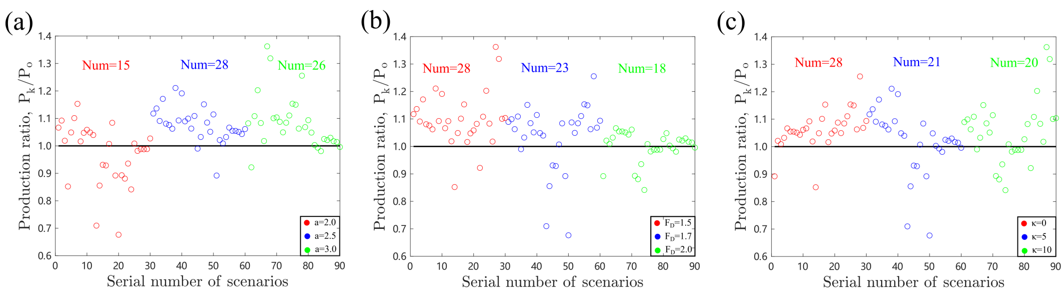

Figure 12. Production ratio between the kinematic fracture networks and the original ones. Different sub-figures classify the production ratio based on the geometrical parameters: (a) the power-law exponent a; (b) the fractal dimension F_D; (c) the concentration parameter κ. The number of cases with the ratio larger than 1.0 is denoted.

Fig. 13 shows similar sensitivity analyses with different responses, including the cumulative gas production of original and kinematic fracture networks and the production ratio between these two types of fracture networks. Compared with the sensitivity results on permeability in Fig. 11, the exponent a and concentration parameter κ have similar results, positive correlations with the cumulative gas production in both kinematic and original fracture networks. However, the fractal dimension F_D has a positive correlation, indicating that clustering effects cannot increase the gas production, and this impact is more signification in the original fracture networks. In Fig. 13(c), the sensitivity results are consistent with the observations in Fig. 12 with a positive correlation for a, a negative correlation for F_D and a weak negative correlation for κ.

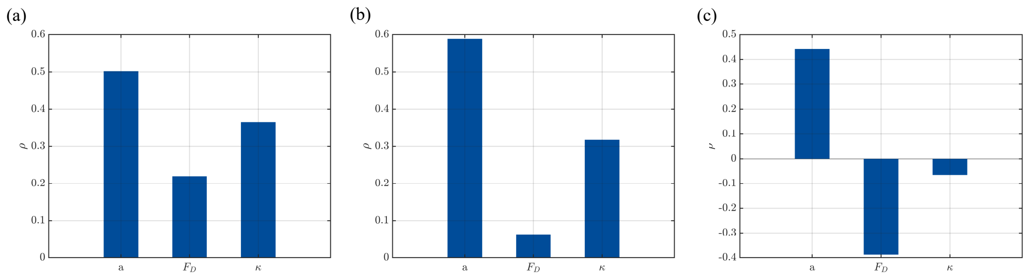

Figure 13. Sensitivity analysis of fracture geometries with (a): cumulative gas production in origin fracture networks; (b): cumulative gas production in growth fracture networks; (c): cumulative gas production ratio between origin and growth fracture networks as responses. ρ is the correlation coefficient between the parameter and the response.

Most kinematic fracture networks have better permeability or cumulative gas production than original ones, and the corresponding proportions are 68% and 77%, respectively. However, the percentage of cases with a connectivity enhancement in kinematic fracture networks is almost 100%. Therefore, flow behaviors and connectivity of fracture networks are correlated but nonequivalent, and flow results are not good candidates to evaluate the connectivity of complex fracture networks as dissuaded in *Zhu et al.* [2021c]. The flow behaviors, such as permeability or fluid production, can be affected by the other geometrical configurations and different boundary conditions. Here, the impact of the number of inlets and outlets is investigated with available data. For single-phase flow, the number of inlets and outlets is the number of fractures intersecting the left and right boundaries. All fractures serve as inlet fractures for the two-phase flow, and the outlets are fractures intersecting the production well in the middle of the formation.

The correlations are summarized in Table 3. Possible influential parameters in both kinematic and original fracture networks include the number of inlets and outlets for the single-phase flow, the number of outlets for the two-phase flow, and the connectivity index.

Table 3. Correlation coefficients between different parameters and responses

Response / Parameter	Permeability (Original)	Permeability (Kinematic)	Ratio of permeability	Cumulative production Original	Cumulative production Kinematic	Ratio of production
No. inlets^{SP} (Original)	0.78	×	0.49	×	×	×
No. inlets^{SP} (Kinematic)	×	0.97	0.48	×	×	×
No. outlets^{SP} (Original)	0.90	×	0.10	×	×	×
No. outlets^{SP} (Kinematic)	×	0.97	0.37	×	×	×
No. outlets^{TP} (Original)	×	×	×	0.74	×	0.16
No. outlets^{TP} (Kinematic)	×	×	×	×	0.69	0.30
Connectivity index (Original)	0.61	×	0.71	0.65	×	0.58
Connectivity index (Kinematic)	×	0.63	0.67	×	0.85	0.54

SP: single-phase flow simulation; TP: two-phase flow simulation

The responses include the permeability of kinematic and original fracture networks, the cumulative gas production of kinematic and original fracture networks, and the ratios of permeability and cumulative production of these two types of fracture networks.

The parameters listed in Table 3 are not included in the sensitivity analysis of geometrical parameters because they are not independent of each other. For example, the number of inlets/outlets depends on the connectivity index, which correlates with geometrical parameters (a, F_D and κ). From the correlation coefficients shown in Table 3, the connectivity index has a positive correlation with flow results, including the permeability and cumulative production, indicating better connectivity of a fracture network can lead to a better flow performance. However, the number of inlets/outlets is also strongly correlated with the flow results, even with a higher correlation coefficient than the connectivity index. For the permeability calculation in the original fracture networks, the correlation coefficients of the number of inlets/outlets are 0.78 and 0.90, respectively. In the kinematic fracture networks, the correlation coefficients are 0.97 for both the number of inlets and outlets. For the cumulative production, the correlations between the number of outlets and cumulative production in the original and kinematic fracture networks are 0.74 and 0.69, respectively. Although the impact of inlets/outlets is not directly comparable with geometrical parameters, it is still qualitatively correct to conclude that the number of inlets and outlets significantly impacts the flow results. The impact of inlets/outlets on the permeability and production ratios is not as significant as the impact on individual permeability and production. Instead, the connectivity index correlates relatively better with permeability and production ratios.

4 Conclusions

In this work, we construct complex fracture networks with their main geometries (fracture lengths, orientations, and center positions) constrained by different stochastic distributions. Multiple levels of geometrical parameters are chosen to make generated fracture networks more representative. By implementing the rule-based fracture growth method, we construct the corresponding kinematic fracture networks, which share the same fracture orientations and fracture intensities (P_{20} and P_{21}) with the original fracture networks. Connectivity and flow results in the original and kinematic fracture networks are systematically analyzed, and several essential conclusions are summarized:

- Kinematic fracture networks tend to connect more fractures with fewer intersections compared with the original fracture networks.
- Kinematic fracture networks systematically have better connectivity than the original fracture networks.
- Most kinematic fracture networks have larger permeability in the single-phase flow simulation and higher cumulative gas production in the two-phase flow simulation than original fracture networks under the same boundary conditions. The proportions of permeability and production enhancement are 68% and 77%, respectively.
- Flow results, like the permeability and production, have strong positive correlations with the connectivity of the fracture networks, but they are nonequivalent and strongly impacted by the number of inlets and outlets.

Data Availability

The original and kinematic fracture networks are generated by an in-house DFN modeling software, HatchFrac. The detailed information about the software can be found at *Zhu et al.* [2021b]. The C++ code for generating 2D and 3D fracture networks and simulating the fracture growth process are available online (https://data.mendeley.com/datasets/zhs97tsdry/1).

Acknowledgments

This project was supported by the National Key Research and Development Program of China (No. 2019YFA0708704). The authors would like to thank Dr. X. Li from Ennosoft for providing the UNCONG simulator to simulate the single-phase and two-phase flow.

The authors would like to thank all editors and anonymous reviewers for their comments and suggestions.

References

Akara, M.-E. M., D. M. Reeves, and R. Parashar (2021), Impact of horizontal spatial clustering in two-dimensional fracture networks on solute transport, *Journal of Hydrology*, *603*, 127,055.

Barton, C., and P. Hsieh (1989), Physical and hydrologic-flow properties of fractures, in *28th International Geological Congress Field Trip Guidebook*, vol. 385, p. 36.

Berkowitz, B. (2002), Characterizing flow and transport in fractured geological media: A review, *Advances in Water Resources*, *25*(8-12), 861–884.

Bonnet, E., O. Bour, N. E. Odling, P. Davy, I. Main, P. Cowie, and B. Berkowitz (2001), Scaling of fracture systems in geological media, *Reviews of geophysics*, *39*(3), 347–383.

Bour, O., and P. Davy (1997a), Connectivity of random fault networks following a power law fault length distribution, *Water Resources Research*, *33*(7), 1567–1583.

Bour, O., and P. Davy (1997b), Connectivity of random fault networks following a power law fault length distribution, *Water Resources Research*, *33*(7), 1567–1583.

Bour, O., and P. Davy (1998), On the connectivity of three-dimensional fault networks, *Water Resources Research*, *34*(10), 2611–2622.

Chen, Z., and M. Wang (2017), Pore-scale modeling of hydromechanical coupled mechanics in hydrofracturing process, *Journal of Geophysical Research: Solid Earth*, *122*(5), 3410–3429.

Darcel, C., O. Bour, P. Davy, and J. De Dreuzy (2003), Connectivity properties of two-dimensional fracture networks with stochastic fractal correlation, *Water resources research*, *39*(10).

Davy, P., R. Le Goc, C. Darcel, O. Bour, J.-R. De Dreuzy, and R. Munier (2010), A likely universal model of fracture scaling and its consequence for crustal hydromechanics, *Journal of Geophysical Research: Solid Earth*, *115*(B10).

Davy, P., R. Le Goc, and C. Darcel (2013), A model of fracture nucleation, growth and arrest, and consequences for fracture density and scaling, *Journal of Geophysical Research: Solid Earth*, *118*(4), 1393–1407.

Dershowitz, W., and H. Einstein (1988), Characterizing rock joint geometry with joint system models, *Rock mechanics and rock engineering*, *21*(1), 21–51.

Ellefsen, K. J., P. A. Hsieh, and A. M. Shapiro (2002), Crosswell seismic investigation of hydraulically conductive, fractured bedrock near mirror lake, new hampshire, *Journal of Applied Geophysics*, *50*(3), 299–317.

Engelder, T. (2004), Tectonic implications drawn from differences in the surface morphology on two joint sets in the Appalachian Valley and Ridge, Virginia, *Geology*, *32*(5), 413–416.

Fadakar-A, Y., C. Xu, and P. Dowd (2013), Connectivity index and connectivity field towards fluid flow in fracture-based geothermal reservoirs, in *Proceedings of 38 Workshop on Geothermal Reservoir Engineering. Stanford University, Stanford, California*, pp. 417–427.

Gierzynski, A. O., and R. M. Pollyea (2017), Three-phase co2 flow in a basalt fracture network, *Water Resources Research*, *53*(11), 8980–8998.

Hardebol, N. J., C. Maier, H. Nick, S. Geiger, G. Bertotti, and H. Boro (2015), Multiscale fracture network characterization and impact on flow: A case study on the latemar carbonate platform, *Journal of Geophysical Research: Solid Earth*, *120*(12), 8197–8222.

Karna, S. K., R. Sahai, et al. (2012), An overview on taguchi method, *International journal of engineering and mathematical sciences*, *1*(1), 1–7.

Kemeny, J., and R. Post (2003), Estimating three-dimensional rock discontinuity orientation from digital images of fracture traces, *Computers & Geosciences*, *29*(1), 65–77.

Laubach, S. E. (1988), Subsurface fractures and their relationship to stress history in east texas basin sandstone, *Tectonophysics*, *156*(1-2), 37–49.

Lei, Q., J.-P. Latham, and C.-F. Tsang (2017), The use of discrete fracture networks for modelling coupled geomechanical and hydrological behaviour of fractured rocks, *Computers and Geotechnics*, *85*, 151–176.

Li, X., D. Zhang, and S. Li (2015), A multi-continuum multiple flow mechanism simulator for unconventional oil and gas recovery, *Journal of Natural Gas Science and Engineering*, *26*, 652–669.

Maillot, J., P. Davy, R. Le Goc, C. Darcel, and J.-R. De Dreuzy (2016), Connectivity, permeability, and channeling in randomly distributed and kinematically defined discrete fracture network models, *Water Resources Research*, *52*(11), 8526–8545.

Nur, A. (1982), The origin of tensile fracture lineaments, *Journal of Structural Geology*, *4*(1), 31–40.

Odling, N. E. (1997), Scaling and connectivity of joint systems in sandstones from western Norway, *Journal of Structural Geology*, *19*(10), 1257–1271.

Olson, J. E. (2004), Predicting fracture swarms-The influence of subcritical crack growth and the crack-tip process zone on joint spacing in rock, *Geological Society, London, Special Publications*, *231*(1), 73–88.

Olson, J. E., S. E. Laubach, and R. H. Lander (2009), Natural fracture characterization in tight gas sandstones: Integrating mechanics and diagenesis, *AAPG bulletin*, *93*(11), 1535–1549.

Prioul, R., and J. Jocker (2009), Fracture characterization at multiple scales using borehole images, sonic logs, and walkaround vertical seismic profile, *AAPG bulletin*, *93*(11), 1503–1516.

Rijks, E., and J. Jauffred (1991), Attribute extraction: An important application in any detailed 3-d interpretation study, *The Leading Edge*, *10*(9), 11–19.

Robinson, P. (1983), Connectivity of fracture systems-a percolation theory approach, *Journal of Physics A: Mathematical and General*, *16*(3), 605.

Sanderson, D. J., and C. W. Nixon (2015), The use of topology in fracture network characterization, *Journal of Structural Geology*, *72*, 55–66.

Segall, P., and D. D. Pollard (1983), Joint formation in granitic rock of the Sierra Nevada, *Geological Society of America Bulletin*, *94*(5), 563–575.

Ukar, E., S. E. Laubach, and J. N. Hooker (2019), Outcrops as guides to subsurface natural fractures: Example from the Nikanassin Formation tight-gas sandstone, Grande Cache, Alberta foothills, Canada, *Marine and Petroleum Geology*, *103*, 255–275.

Wang, M., J. He, J. Yu, and N. Pan (2007), Lattice boltzmann modeling of the effective thermal conductivity for fibrous materials, *International Journal of Thermal Sciences*, *46*(9), 848–855.

Wang, Y., S. de Hoop, D. Voskov, D. Bruhn, and G. Bertotti (2021), Modeling of multiphase mass and heat transfer in fractured high-enthalpy geothermal systems with advanced discrete fracture methodology, *Advances in Water Resources*, *154*, 103,985.

Watkins, H., C. E. Bond, D. Healy, and R. W. Butler (2015), Appraisal of fracture sampling methods and a new workflow to characterise heterogeneous fracture networks at outcrop, *Journal of Structural Geology*, *72*, 67–82.

Whitaker, A. E., and T. Engelder (2005), Characterizing stress fields in the upper crust using joint orientation distributions, *Journal of Structural Geology*, *27*(10), 1778–1787.

Wilt, M., D. Alumbaugh, H. Morrison, A. Becker, K. H. Lee, and M. Deszcz-Pan (1995), Crosswell electromagnetic tomography: System design considerations and field results, *Geophysics*, *60*(3), 871–885.

Xu, C., P. Dowd, K. Mardia, and R. Fowell (2006), A connectivity index for discrete fracture networks, *Mathematical geology*, *38*(5), 611–634.

Zhu, W., S. Khirevich, and T. Patzek (2018), Percolation properties of stochastic fracture networks in 2d and outcrop fracture maps, in *80th EAGE Conference and Exhibition 2018*, vol. 2018, pp. 1–5, European Association of Geoscientists & Engineers.

Zhu, W., X. He, R. K. Santoso, G. Lei, T. Patzek, and M. Wang (2021a), Enhancing fracture network characterization: A data-driven, outcrop-based analysis, *Earth and Space Science Open Archive*, p. 35, doi:10.1002/essoar.10508232.1.

Zhu, W., S. Khirevich, and T. W. Patzek (2021b), Hatchfrac: A fast open-source dfn modeling software, *Earth and Space Science Open Archive*, p. 44, doi:10.1002/essoar.10508657.1.

Zhu, W., S. Khirevich, and T. W. Patzek (2021c), Impact of fracture geometry and topology on the connectivity and flow properties of stochastic fracture networks, *Water Resources Research*, p. e2020WR028652.

Zhu, W., X. He, Y. Li, G. Lei, R. Santoso, and M. Wang (2022), Impacts of fracture properties on the formation and development of stimulated reservoir volume: a global sensitivity analysis, *Earth and Space Science Open Archive*, p. 43.